Chinese Chemical Letters 37 (2026) 111974

Contents lists available at ScienceDirect

Chinese Chemical Letters

journal homepage: www.elsevier.com/locate/cclet

Strong p–d orbital hybridization in Pd-Sb intermetallic nanodisks boosts ethanol electrooxidation

Sumei Han[a,1], Chaoqun Ma[a,1], Fukai Feng[a,1], Xinran Jiao[a], Xiao Ma[a], Caihong He[a], Huaifang Zhang[a], Gang Lin[a], Xiangmin Meng[b], Jing Xia[b,*], Qinbai Yun[c,*], Wenbin Cao[a,*], Qipeng Lu[a,*]

[a] School of Materials Science and Engineering, University of Science and Technology Beijing, Beijing 100083, China
[b] Key Laboratory of Photochemical Conversion and Optoelectronic Materials, Technical Institute of Physics and Chemistry, Chinese Academy of Sciences, Beijing 100190, China
[c] Sustainable Energy and Environment Thrust, The Hong Kong University of Science and Technology (Guangzhou), Guangzhou 511400, China

ARTICLE INFO

Article history:
Received 1 September 2025
Revised 13 October 2025
Accepted 15 October 2025
Available online 17 October 2025

Keywords:
Orbital hybridization
Intermetallic compounds
Ethanol oxidation
Reaction pathway
Nanodisks

ABSTRACT

Palladium (Pd)-based catalysts are commonly used for ethanol oxidation reaction (EOR) in direct ethanol fuel cells, but their performance is hindered by sluggish kinetics and CO poisoning. Engineering p-d orbital hybridization between p-block metals and Pd can optimize the electronic properties and thus boosting the electrocatalytic activities. Therefore, Pd_8Sb_3 intermetallic nanodisks (NDs) with an unconventional trigonal phase are synthesized through a simple hydrothermal method, promoting a strong p-d hybridization between Pd and Sb. These Pd_8Sb_3 NDs exhibit exceptional EOR performance with a mass activity of 4.6 A/mg, approximately six times as high as commercial Pd/C. Density functional theory (DFT) calculations confirm that p-d hybridization optimizes intermediates adsorption and reduces reaction energy barriers. This work provides an effective pathway to fabricate strong p-d orbital hybridization and enhance the catalytic performance of Pd-based catalysts for renewable energy applications.

© 2026 Published by Elsevier B.V. on behalf of Chinese Chemical Society and Institute of Materia Medica, Chinese Academy of Medical Sciences.

With energy crisis increasing and pollution spreading, the need for renewable energy technologies is growing [1]. Among them, direct ethanol fuel cells have garnered significant attention due to their high theoretical energy density, low toxicity, and easy accessibility from biomass [2,3]. Previous studies have demonstrated that Pd-based materials are widely used catalysts for ethanol oxidation reaction (EOR), which is the anodic reaction of direct ethanol fuel cells [4–7]. However, during the EOR process the multiple electron pathways lead to sluggish kinetics and the formation of intermediate by-products such as CO easily deactivates the Pd catalyst. In addition, the high cost of Pd limits their large-scale application in EOR. Therefore, Pd-based electrocatalysts with outstanding catalytic ability are still urgently needed.

In order to modulate the configurations of Pd sites, introducing p-block elements into Pd is an effective strategy. The higher energy of p-orbitals compared to d-orbitals suggests that p-d hybridization may be a more effective strategy for modulation than d-d hybridization by alloying with d-block metals in terms of orbital energy [8–12]. At present, the common strategies to introduce p-d hybridization include constructing Pd-based alloys with p-block metals or metalloids, and doping p-block elements into metallic Pd [13–15]. However, the disordered arrangement of Pd and p-block metals in these catalysts makes the p-d hybridization distribute unevenly, limiting the fine modulation of electronic structure of the electrocatalyst. In contrast, Pd-based intermetallics containing p-block metals or metalloids exhibit an ordered atomic configuration and specific atomic bonding between Pd and p-block metals or metalloids [16–18]. But the influence of p-d hybridization in Pd-based intermetallics on the catalytic performance are neglected [17,19]. In addition, the generally used thermal annealing method leads to aggregation and destroys the morphology of nanocatalysts in many cases, decreasing the exposed active sites and reducing the catalytic performance [20–22]. Therefore, preparing Pd-based intermetallics containing p-block metals through a simple wet-chemical strategy and investigating the effect of p-d hybridization are highly desired.

In this work, we successfully synthesized intermetallic Pd_8Sb_3 nanodisks (NDs) with an average diameter of 19.5 nm and a thickness of only 3.2 nm through a straightforward one-step hydrother-

* Corresponding authors.
E-mail addresses: xiajing@mail.ipc.ac.cn (J. Xia), qinbaiyun@hkust-gz.edu.cn (Q. Yun), wbcao@ustb.edu.cn (W. Cao), qipeng@ustb.edu.cn (Q. Lu).
[1] These authors contributed equally to this work.

https://doi.org/10.1016/j.cclet.2025.111974
1001-8417/© 2026 Published by Elsevier B.V. on behalf of Chinese Chemical Society and Institute of Materia Medica, Chinese Academy of Medical Sciences.

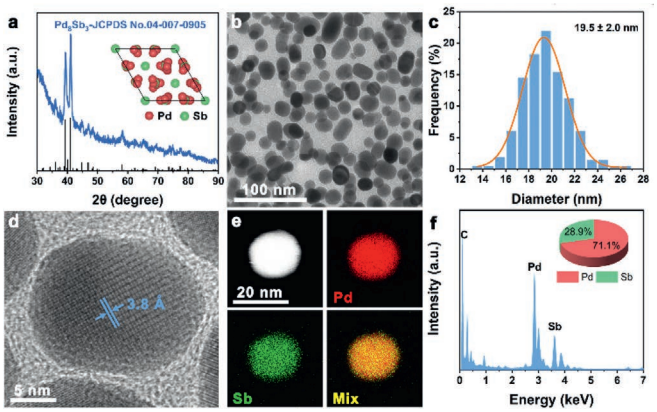


Fig. 1. (a) XRD pattern of Pd_8Sb_3 NDs. The inset illustrates the corresponding crystal structure model. (b) TEM image and (c) diameter distribution of Pd_8Sb_3 NDs. (d) HRTEM image, (e) EDS mapping and (f) EDS spectrum of Pd_8Sb_3 NDs.

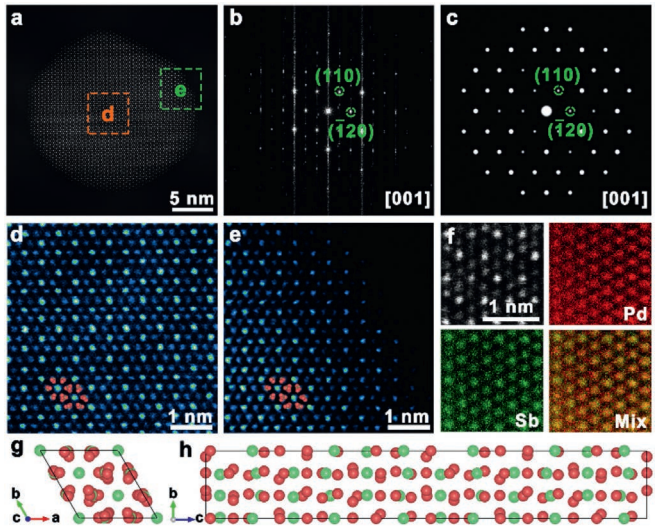


Fig. 2. (a) HAADF-STEM image of a single Pd_8Sb_3 ND. (b) The corresponding FFT pattern of (a). (c) The simulated FFT pattern of Pd_8Sb_3 intermetallic along [001] direction. (d, e) The high-resolution HAADF-STEM image taken from areas marked in (a). (f) Atomic-resolution elemental mappings of a Pd_8Sb_3 ND. Crystal structure model viewed along the (g) [001] and (h) [100] directions. Red and green spheres denote Pd and Sb atoms, respectively.

mal process. The ordered atomic arrangement within the intermetallic Pd_8Sb_3 NDs facilitate the strong p-d orbital hybridization of Pd and Sb atoms. The Pd_8Sb_3 NDs deliver an excellent EOR performance with a mass activity (MA) of 4.6 A/mg, approximately 6 times as high as that of commercial Pd/C. Furthermore, the unconventional p-d orbital hybridization of Pd and Sb atoms has been successfully established according to the density functional theory (DFT) calculations. This unique electronic interaction significantly enhances the catalytic performance by optimizing the adsorption energy of reaction intermediates and lowering the energy barriers for key reaction steps. Our findings elucidate the relationship between electronic interaction modulation and EOR activity in Pd-based intermetallics, and provide valuable guidance for designing highly efficient catalysts.

The intermetallic Pd_8Sb_3 nanodomains (NDs) are fabricated through a hydrothermal synthesis approach. In this method, palladium(II) acetylacetonate ($Pd(acac)_2$) and antimony trichloride ($SbCl_3$) served as the primary metal precursors. Poly(vinylpyrrolidone) (PVP) was employed as a stabilizing surfactant, while ethylene glycol acted as the reaction solvent. Further details of the synthesis procedure are provided in Supporting information. The X-ray diffraction (XRD) pattern (Fig. 1a) reveals the highly crystalline of the products, exhibiting an intermetallic Pd_8Sb_3 phase (JCPDS No. 04–007–0905) with regular atomic arrangement of Pd and Sb (inset in Fig. 1a), which belongs to the trigonal $R\bar{3}c$ space group. Transmission electron microscope (TEM) image demonstrates that uniform Pd_8Sb_3 NDs are obtained (Fig. 1b). Statistical analysis reveals that the average diameter of Pd_8Sb_3 NDs is approximately 19.5 nm (Fig. 1c). Atomic force microscopy (AFM) analysis indicates that the Pd_8Sb_3 NDs have a thickness of approximately 3.2 nm (Fig. S1 in Supporting information), which is smaller than their diameter, indicating the disk-like morphology of the obtained samples. Moreover, the thickness at the center of the NDs is greater than that at the edge. The lattice spacing of 3.8 Å observed in the high-resolution TEM (HRTEM) image is characteristic of the (300) plane of Pd_8Sb_3, thereby verifying the successful synthesis of intermetallic Pd_8Sb_3 phase (Fig. 1d). Elemental mapping images obtained *via* high-angle annular dark-field scanning transmission electron microscope energy-dispersive X-ray spectroscopy (HAADF-STEM-EDS) reveal uniform distribution of Pd and Sb elements across the NDs (Fig. 1e), consistent with the EDS line scanning profile (Fig. S2 in Supporting information)). The atomic ratio of Pd to Sb in the NDs is approximately 71.1:28.9 from HAADF-STEM EDS (Fig. 1f). This ratio aligns closely with the ratio obtained from inductively coupled plasma optical emission spectrometry (ICP-OES), which measured a Pd:Sb ratio of 72.3:27.7.

To investigate the atomic structure of Pd_8Sb_3 NDs, aberration-corrected HAADF-STEM characterization is conducted. The ordered arrangement of atoms is clearly visible (Fig. 2a). The corresponding fast Fourier transform (FFT) pattern of Fig. 2a is displayed in Fig. 2b, in which the diffraction pattern is consistent with the simulated FFT pattern of trigonal Pd_8Sb_3 along the [001] zone axis (Fig. 2c). The (110) superlattice spot observed in Fig. 2b further demonstrates the formation of the trigonal Pd_8Sb_3 phase. Furthermore, the magnified views of regions d and e in Fig. 2a (Figs. 2d and e) reveal atomic columns with distinct contrasts. The atomic structure is consistent with the trigonal Pd_8Sb_3 phase, belonging to the $R\bar{3}c$ space group. The Pd and Sb atoms are located in different atomic columns, as shown in the HAADF-STEM image with atomic-resolution elemental mappings (Fig. 2f), line scanning profile (Fig. S3 in Supporting information) and the atomic models of Pd_8Sb_3 (Figs. 2g and h). Therefore, the contrast variation cannot be only attributed to the atomic number (Z) of Pd ($Z = 46$) and Sb ($Z = 51$). The variation in the number of Pd and Sb atoms within distinct atomic columns also accounts for the contrast differences observed in Figs. 2d and e.

To uncover the formation mechanism of Pd_8Sb_3 NDs, a series of products obtained at various reaction time are analyzed using XRD and TEM. As shown in the XRD patterns of the products (Fig. S4 in Supporting information), when the reaction time is 15 min, the products contain Pd_8Sb_3 intermetallic compound and face-centered cubic (*fcc*) Pd. This result indicates that Pd is reduced first at the initial stage. As the reaction time increases, more Sb is reduced to form the Pd_8Sb_3 intermetallic compound. As a result, the peak of Pd at 40.1° gradually disappears while the signal of Pd_8Sb_3 intermetallic compound becomes more pronounced. Additionally, an increase in reaction time from 15 min to 120 min results in an enlargement of the product particle size from 10.6 nm to 19.6 nm (Fig. S5 in Supporting information). Apart from reaction time, reaction temperature also plays a crucial role in the synthesis of intermetallic compound as a high temperature could provide sufficient energy to overcome the atomic diffusion energy barrier to induce ordered atomic arrangement. Consequently, only a Pd–Sb solid solution is obtained when the reaction temperatures are 120 °C or 140 °C (Fig. S6 in Supporting information). However, Pd_8Sb_3 inter-

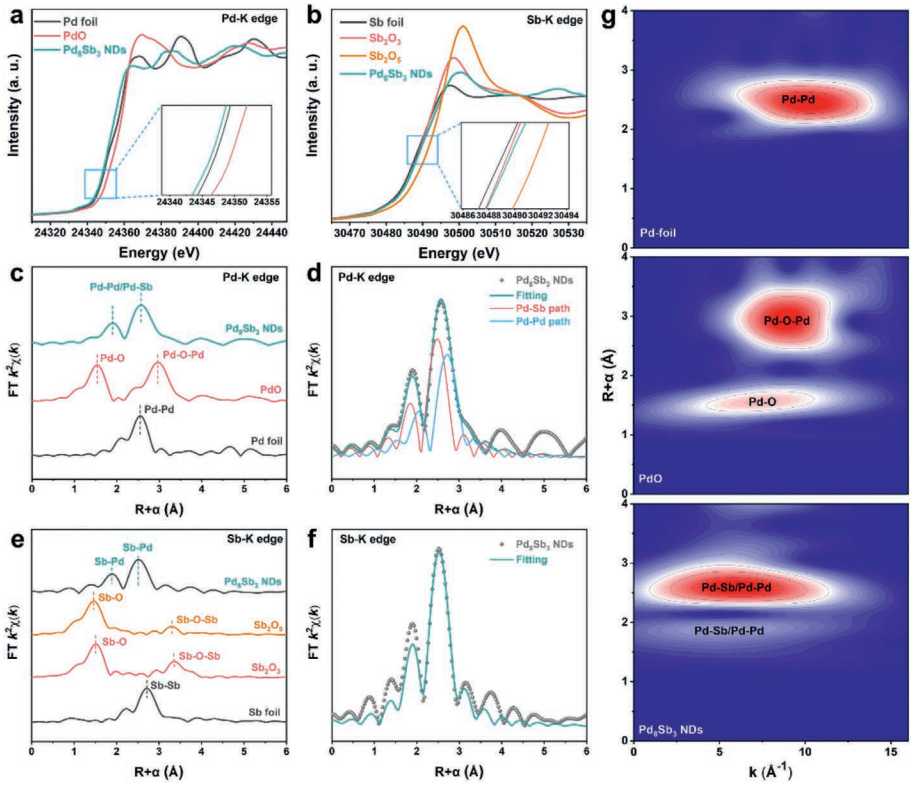


Fig. 3. (a) Normalized XANES spectra at the Pd K-edge of Pd_8Sb_3 NDs, Pd foil, and PdO. (b) Normalized XANES spectra at the Sb K-edge of Pd_8Sb_3 NDs, Sb foil, Sb_2O_3, and Sb_2O_5. (c) Pd K-edge FT-EXAFS spectra of Pd_8Sb_3 NDs, Pd foil, and PdO. (d) EXAFS fitting curves at the Pd K-edge of Pd_8Sb_3 NDs. (e) Sb K-edge FT-EXAFS spectra of Pd_8Sb_3 NDs, Sb foil, Sb_2O_3, and Sb_2O_5. (f) EXAFS fitting curve at the Sb K-edge of Pd_8Sb_3 NDs. (g) WT-EXAFS contour plots of Pd_8Sb_3 NDs and the reference samples.

metallic compound forms when the reaction temperature exceeds 160 °C. These control experiments demonstrate that appropriate reaction time and temperature are essential for the synthesis of pure Pd_8Sb_3 intermetallic NDs. To unravel the chemical states of elements in the synthesized Pd_8Sb_3 NDs, X-ray photoelectron spectroscopy (XPS) characterization is conducted. Prior to the XPS analysis, Pd_8Sb_3 NDs are loaded on commercial carbon (named Pd_8Sb_3 NDs/C) to compare the binding energy with that of commercial Pd/C. Pd and Sb are present in the Pd_8Sb_3 NDs (Fig. S7a in Supporting information). The Pd 3d peaks in Fig. S7b (Supporting information) indicate that Pd is primarily in the metallic state. Notably, the Pd^0 peaks of Pd_8Sb_3 NDs/C shift negatively by 0.59 eV compared to those of Pd/C (Fig. S7c in Supporting information), indicating the electron donation from Sb to Pd atoms due to the lower electronegativity of Sb (2.05) than that of Pd (2.20) [23,24]. Compared to Pd/C, Pd_8Sb_3 has a lower proportion of oxidized Pd, attributing to the alloying effect in Pd_8Sb_3 intermetallic compound that inhibits the oxidation of Pd. In addition, the Sb 3d peaks in Fig. S7d (Supporting information) show that Sb also mainly exists in the metallic state. The O 1s peak in the Sb 3d XPS spectrum can be deconvoluted into three characteristic peaks (*i.e.*, O_I at 530.7 eV, O_{II} at 532.1 eV, and O_{III} at 533.8 eV). These peaks are attributed to lattice oxygen in metal oxides, defect-oxide/hydroxyl–like groups, and oxide in adsorbed or residual water molecules, respectively [25].

The electronic structures of Pd and Sb are further investigated using the X-ray absorption near-edge fine structure (XANES) measurements. Fig. 3a shows the K-edge XANES spectra of Pd_8Sb_3 NDs with Pd foil and PdO as references. The adsorption edge of Pd_8Sb_3 NDs shifts negatively compared to Pd foil and PdO, suggesting an increase in electron density at the Pd sites. Conversely, the white line intensity of the Sb K-edge in Fig. 3b is higher than that of Sb foil, indicating a decrease in electron density around Sb sites. Meanwhile, the adsorption threshold of Pd_8Sb_3 NDs is higher than those of Sb foil and Sb_2O_3 but lower than that of Sb_2O_5, illustrating that the valence state of Sb is between Sb^{3+} and Sb^{5+}. The above results suggest the electron transfer from Sb to Pd because of the p-d orbital hybridization in Pd_8Sb_3 NDs. The coordination environment of Pd and Sb in Pd_8Sb_3 NDs is elucidated through Fourier-transformed extended X-ray absorption fine structure (FT-EXAFS) spectra. In Fig. 3c, a distinct signal centered at ≈ 2.74 Å in the FT-EXAFS spectrum of Pd K-edge in Pd_8Sb_3 NDs is observed, which is near the position of Pd–Pd bond in Pd foil. No signal of Pd–O bond exists in Pd_8Sb_3 NDs, in contrast to the obvious peak of Pd–O bond in PdO. The FT-EXAFS spectrum of Pd K-edge in Pd_8Sb_3 NDs could be fitted by the Pd–Pd path (≈ 2.70 Å) and Pd–Sb path (≈ 2.49 Å) as shown in Fig. 3d, with the fitted data provided in Table S1. Notably, the small peak at ≈ 1.90 Å could be assigned to the Pd–Sb bond and Pd–Pd bond as well. It should be noted that the presence of multiple Pd–Sb and Pd–Pd shells is expected to lead to the spectral cancellation due to destructive interference of the respective EXAFS oscillations [26]. Therefore, the coordination number of Pd is underestimated. However, the trends in relative coordination numbers and the bonding of atoms remain consistent. From the FT-EXAFS spectrum of Pd K-edge and corresponding fitting result, we can conclude that Pd–Sb bond exists in Pd_8Sb_3 NDs. In the Sb K-edge FT-EXAFS spectra of Pd_8Sb_3 NDs (Fig. 3e), a peak located at 2.68 Å is attributed to the Sb–Pd bond, which is distinct from the Sb–Sb bond in Sb foil (2.91 Å), and the Sb–O bond in Sb_2O_3 (1.50 Å) and Sb_2O_5 (1.46 Å). The least-squares EXAFS fitting results are displayed in Fig. 3f and Table S2 (Supporting information). The Pd K-edge wavelet transform EXAFS (WT-EXAFS) spectra of Pd_8Sb_3 NDs differ from those of Pd foil and PdO, indicating a different coordination environment (Fig. 3g). In the WT-EXAFS of Pd K-edge in Pd_8Sb_3 NDs, the strong signal at $k = 5.0$ Å^{-1} could be assigned to the Pd–Pd and Pd–Sb bonds, based on the comparisons with the

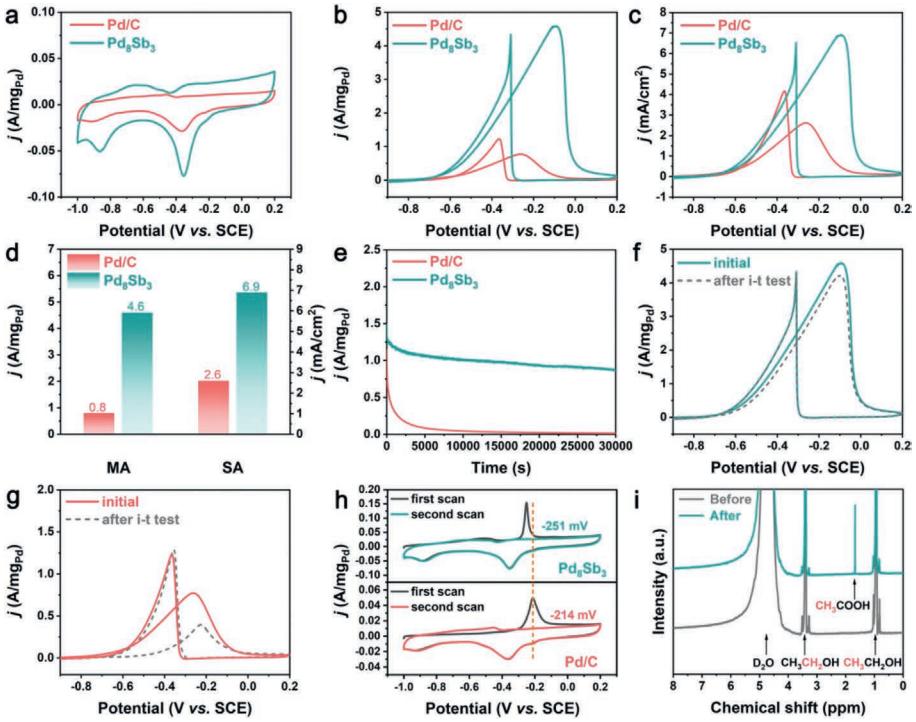


Fig. 4. (a) CV curves of Pd_8Sb_3 NDs and commercial Pd/C tested in a 1.0 mol/L KOH aqueous solution. CV curves normalized to (b) the mass of Pd and (c) ECSAs tested in 1.0 mol/L KOH + 1.0 mol/L ethanol. (d) Histogram of mass activities (MAs) and specific activities (SAs) for EOR. (e) *i-t*-test of Pd_8Sb_3 NDs and Pd/C recorded at −0.3 V (*vs.* SCE). CV curves of (f) Pd_8Sb_3 NDs and (g) Pd/C before and after the *i-t*-test. (h) CO-stripping measurements of different catalysts in 1.0 mol/L KOH (scan rate: 50 mV/s). (i) ^{1}H NMR spectra of the electrolytes before and after *i-t*-test.

Pd–Pd and Pd–O–Pd signals in Pd foil and PdO. In the WT-EXAFS spectra of Sb K-edge in Pd_8Sb_3 NDs (Fig. S8a in Supporting information), only one strong signal observed at 7.6 Å^{-1} is attributed to Pd–Sb bond. The position shifts negatively compared to the signal of Sb–Sb bond in Sb foil (Fig. S8b in Supporting information), and shifts positively compared to the signal of Sb–O–Sb bond in Sb_2O_3 and Sb_2O_5 (Figs. S8c and d in Supporting information). The above results confirm the presence of Pd–Sb bond in the Pd_8Sb_3 NDs and Sb atoms donate electrons to Pd atoms because of the p-d orbital hybridization.

Given that Pd-based nanomaterials are widely acknowledged as highly promising anode catalysts for direct alcohol fuel cells (DAFCs) under alkaline conditions, our prepared Pd_8Sb_3 NDs are employed as electrocatalyst for EOR in alkaline conditions. Prior to the evaluation of electrocatalytic performance, Pd_8Sb_3 NDs are loaded on commercial carbon black (*i.e.*, Ketjen Black) to prepare the carbon-supported electrocatalysts. Commercial Pd/C is also tested under the same conditions for comparison. Fig. 4a illustrates the cyclic voltammograms (CVs) of Pd_8Sb_3 NDs and commercial Pd/C in 1.0 mol/L KOH. The reduction peaks located at about −0.35 V (*vs.* saturated calomel electrode (SCE)) are attributed to the reduction peak of PdO. The stronger reduction peak of PdO in Pd_8Sb_3 compared to that in Pd/C suggests the more exposed Pd active sites for catalytic reaction. The integrated charge associated with the reduction peak is used to estimate the electrochemical surface areas (ECSAs) of Pd_8Sb_3 NDs and Pd/C. Pd_8Sb_3 NDs possess a larger ECSA (66.4 m^2/g) than that of commercial Pd/C (29.5 m^2/g), indicating much higher utilization efficiency of Pd in Pd_8Sb_3 NDs. As shown in Figs. 4b and c, CV curves are further recorded in 1.0 mol/L KOH + 1.0 mol/L ethanol to assess the catalytic activities of the catalysts. Impressively, the MA and specific activity (SA) of Pd_8Sb_3 NDs significantly increases compared to that of commercial Pd/C. Notably, Pd_8Sb_3 NDs possess a MA of 4.6 A/mg, which is about 6 times as high as that of commercial Pd/C (Fig. 4d, left). And the SAs of Pd_8Sb_3 NDs and commercial Pd/C are 6.9 and 2.6 A/cm^2, respectively (Fig. 4d, right). As displayed in Table S3, the MA of Pd_8Sb_3 NDs outperforms most of the reported Pd-based electrocatalysts. Meanwhile, the onset potential of EOR on Pd_8Sb_3 NDs is 70 mV lower than that on Pd/C (Fig. S9 in Supporting information), indicating that the reaction kinetics of EOR is facilitated on Pd_8Sb_3 NDs. These results indicate that Pd_8Sb_3 NDs exhibit excellent catalytic performance towards EOR.

Apart from catalytic activity, the stability of the catalysts during the EOR process is crucial as well. To evaluate the durability of highly active Pd_8Sb_3 NDs, long-term *i-t* measurements are conducted at −0.3 V (*vs.* SCE) for 30,000 s. As shown in Fig. 4e, the MA of Pd_8Sb_3 NDs remains 0.9 A/mg after the *i-t*-test while the MA of commercial Pd/C decreases rapidly, nearly losing the mass activity. In addition, after 30,000 s, the current density of Pd_8Sb_3 NDs only decays by 8.7 %, compared to a 51.2 % decrease for commercial Pd/C (Figs. 4f and g), further demonstrating the superior stability of Pd_8Sb_3 NDs. Besides, no obvious change is found from the TEM image, the XRD pattern, and the EDS mapping of the Pd_8Sb_3 NDs after the *i-t*-test (Fig. S10 in Supporting information), demonstrating the high stability on the crystal structure and composition. Meanwhile, the atomic ratio of Pd and Sb is 73.1:26.9 after the *i-t*-test (Table S4 in Supporting information), close to the atomic ratio of the synthesized Pd_8Sb_3 NDs. This result indicates negligible Sb dissolution occurs during the long-term stability test. And the Pd and Sb are still mainly in the metallic state (Fig. S11 in Supporting information), further demonstrating the structural stability of Pd_8Sb_3 NDs. It is widely acknowledged that CO-induced poisoning of Pd active sites is unavoidable during the EOR [19,27]. The ratio of forward current density to backward current density (I_f/I_b) indicates the resistance of catalysts to poisoning by reaction intermediates. As shown in Fig. 4b, Pd_8Sb_3 NDs possess an I_f/I_b value of 1.06, larger than that of commercial Pd/C (0.63), revealing the good tolerance ability to intermediates. To further confirm

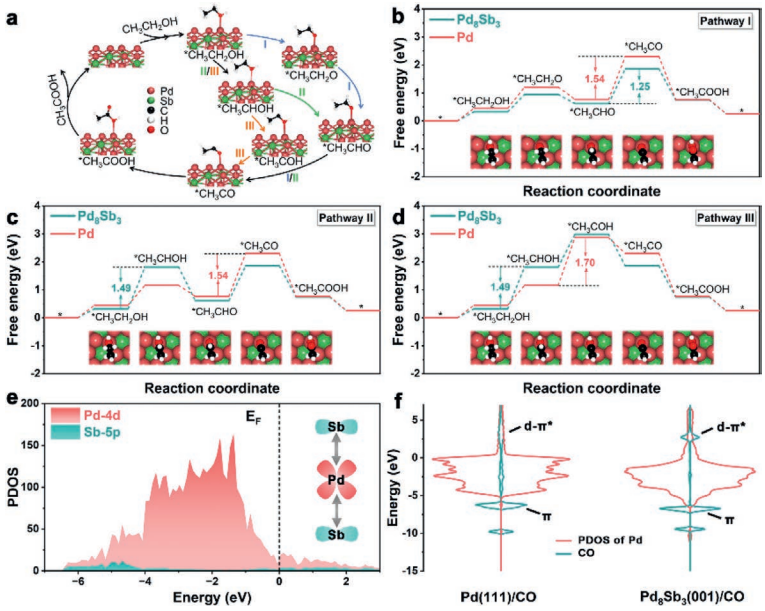


Fig. 5. (a) The scheme of reaction pathways on Pd_8Sb_3 (001). Free energy profiles of EOR on Pd_8Sb_3 (001) and Pd (111) through (b) Pathway I, (c) Pathway II and (d) Pathway III. (e) The PDOS of Pd_8Sb_3 (001). (f) The interaction between CO molecule and Pd 3d orbital in Pd (111) and Pd_8Sb_3 (001).

the improved anti-poisoning ability of Pd_8Sb_3 NDs, CO stripping experiments are conducted. The peak potential of CO oxidation on Pd_8Sb_3 NDs (−251 mV) is 37 mV more negative than that of commercial Pd/C (−214 mV), indicating the easier removal of CO from Pd_8Sb_3 NDs and their substantially enhanced CO tolerance (Fig. 4h) [28,29]. Previous work has reported that Sb can form oxidation species at low potential, facilitating the oxidation of CO adsorbed on adjacent Pd site [25,30]. To investigate the product of EOR on Pd_8Sb_3 NDs, ^{1}H nuclear magnetic resonance (NMR) spectra of the electrolytes are measured before and after *i-t*-test. As shown in Fig. 4i, before electrolysis, the signals of H atoms in terminal hydroxymethyl (-CH_2OH) and methyl (-CH_3) groups of CH_3CH_2OH are observed clearly at 3.64 and 1.15 ppm, respectively. After the *i-t*-test, an obvious NMR signal appears at 1.76 ppm, indicating that acetic acid (CH_3COOH) is the only liquid product after EOR. Furthermore, the Faradaic efficiency of the acetic acid is calculated based on the calibration curve method and the standard curve is shown in Fig. S12 (Supporting information). The Faradaic efficiency of the acetic acid for Pd_8Sb_3 NDs is 80.7 %, confirming that EOR on Pd_8Sb_3 NDs mainly proceed through the C2 pathway with 4 electrons transfer.

To shed light on the superior EOR performance of Pd_8Sb_3 intermetallic NDs, DFT calculations are carried out (see Supporting Information for computational details). Two typical models, including Pd (111) surface and Pd_8Sb_3 (001) surface are constructed for the calculations (Fig. S13 in Supporting information). Based on the NMR results, the main product of EOR on Pd_8Sb_3 is CH_3COO^-. During the EOR process, multiple intermediates are generated, indicating different reaction pathways [31]. To elucidate the reaction mechanism, three possible pathways and corresponding models are shown in Fig. 5a and Fig. S14 (Supporting information) [32]. In Pathway I, the O–H bond is first broken, leading to the formation of $^*CH_3CH_2O$ intermediates, and the C–H bond in -CH_2 is further broken to form $^*CH_3CHO$. In Pathway II and Pathway III, the C–H bond, rather than O–H bond, is dissociated to form $^*CH_3CHOH$. After that, the O–H bond is broken, resulting in the formation of $^*CH_3CHO$ in Pathway II, while $^*CH_3COH$ is obtained after further dissociation of C–H bond in Pathway III. Figs. 5b-d illustrate the free energies of intermediates adsorbed on Pd_8Sb_3 (001) and Pd (111). Obviously, in Pathway I, the potential determining step (PDS) on Pd_8Sb_3 (001) is the oxidation of $^*CH_3CHO$ to $^*CH_3CO$, which requires 1.25 eV to overcome the energy barrier. In both Pathway II and III, the PDS on Pd_8Sb_3 (001) is the dehydrogenation of $^*CH_3CH_2O$ to $^*CH_3COH$, with a higher energy barrier of 1.49 eV. The above results demonstrate that EOR follows Pathway I on Pd_8Sb_3 (001). As for Pd (111), the required energies for PDS in Pathway I, II and III are 1.54, 1.54 and 1.70 eV, respectively, all of which are higher than those required on Pd_8Sb_3 (001). To identify the factors contributing to the enhanced electrocatalytic activity of Pd_8Sb_3 (001) in EOR, we investigate the electronic structure and the binding energies of key intermediates using theoretical calculations. As shown in the total density of states of Pd_8Sb_3 (001), high electronic states at the Fermi level are observed, suggesting the metallic characteristic of the catalyst (Fig. S15 in Supporting information) [33,34]. Therefore, Pd_8Sb_3 NDs possess high conductivity during the EOR, benefiting the catalytic activity. Moreover, the projected DOS (PDOS) of Pd_8Sb_3 in Fig. 5e illustrates that the peaks of Pd 4d orbitals closely overlap with those of Sb 5p orbitals. This, combined with the absence of Sb 4d orbitals (Fig. S16 in Supporting information), suggests the strong p-d orbital hybridization between Pd and Sb, as opposed to weaker d-d interactions [8,13,35]. From the differential charge distribution on Pd_8Sb_3 (001) (Fig. S17a in Supporting information), the redistribution of electrons of Pd induced by the p-d orbital hybridization is observed, indicating the charge transfer between Pd and Sb atoms. Through Bader charge analysis, it is shown that each Pd atom obtains an average of 0.308 |e| electrons from the Sb (Fig. S17b in Supporting information), aligning with the XPS and XANES results. The change of electronic configuration determines the adsorption energy of the key intermediates, thereby tuning the catalytic activity of catalysts. For example, the adsorption energy of CH_3CH_2OH and $^*OH$ on Pd_8Sb_3 (001) is −0.33 eV and 0.65 eV, respectively, which are lower than those on Pd (111) (−0.20 and 0.94 eV) as shown in Fig. S18 (Supporting information), confirming the easier adsorption of CH_3CH_2OH and $^*OH$ on Pd_8Sb_3. The d-band center of Pd_8Sb_3 (001) (−2.21 eV) shifts negatively compared with that of Pd (111) (−1.80 eV), making it easier to adsorb CH_3CH_2OH and $^*OH$ on Pd_8Sb_3 NDs (Fig. S19 in Supporting information). This result is consistent with the calculated adsorption energies of CH_3CH_2OH and $^*OH$ on Pd_8Sb_3 (001) and Pd (111). The easier adsorption of CH_3CH_2OH on Pd_8Sb_3 facilitates the first step of EOR. And the en-

hanced •OH adsorption benefits the removal of poisoning intermediates such as CO, which is consistent with the results of CO-stripping test. In addition, the adsorption energy of CO on Pd_8Sb_3 (001) is higher than that on Pd (111), indicating the weaker CO bonding. Furthermore, to investigate the bonding behavior of CO, the DOS of CO adsorbed on Pd (111) and Pd_8Sb_3 (001) are calculated (Fig. 5f). Clearly, the interaction of the bonding (π) and anti-bonding (π^*) orbitals in CO are different over Pd and Pd_8Sb_3. The energy levels of CO π orbitals match more well with Cu 3d orbitals of Pd in Pd (111) than in Pd_8Sb_3 (001). And the energy dispersity of d-π^* in Pd (111)/CO is broader than that in Pd_8Sb_3 (001)/CO above the Fermi level. The above results illustrate that the p-d hybridization in Pd_8Sb_3 changes the electronic structure of Pd, which can reduce the adsorption of CO and thus benefit for the anti-poisoning ability. Overall, the preparation of intermetallic Pd_8Sb_3 NDs by incorporating p-block Sb with d-block Pd leads to the transition from d-d hybridization of the *fcc* Pd (111) surface to p-d hybridization of the trigonal Pd_8Sb_3 (001) surface. This change allows for the reconfiguration of electrons, which optimize the intrinsic adsorption properties for key intermediates. As a result, Pd_8Sb_3 NDs exhibit superior catalytic activity than commercial Pd/C.

In summary, intermetallic Pd_8Sb_3 NDs with a trigonal crystal structure have been synthesized using a simple hydrothermal strategy. A strong p-d orbital hybridization interaction is present in intermetallic Pd_8Sb_3 NDs. The synthesized intermetallic Pd_8Sb_3 NDs exhibit outstanding EOR performance with a MA of 4.6 A/mg, which is about 6 times as high as that of commercial Pd/C. The intermetallic Pd_8Sb_3 NDs also possess an improved stability after the *i-t*-test for 30,000 s with a slight decay of 8.7 % in current density, as well as strong resistance to CO poisoning. DFT calculation results demonstrate that the intermetallic Pd_8Sb_3 NDs reduce the energy barrier of the PDS in EOR. Meanwhile, the p-d orbital hybridization interaction in intermetallic Pd_8Sb_3 NDs modifies the electronic structure, thereby optimizing the adsorption/desorption energies with the key intermediates.

CRediT authorship contribution statement

Sumei Han: Writing – original draft, Investigation, Formal analysis, Data curation, Conceptualization. **Chaoqun Ma:** Visualization, Software, Data curation. **Fukai Feng:** Visualization, Methodology, Investigation. **Xinran Jiao:** Data curation. **Xiao Ma:** Validation. **Caihong He:** Formal analysis. **Huaifang Zhang:** Validation. **Gang Lin:** Visualization. **Xiangmin Meng:** Software, Funding acquisition. **Jing Xia:** Supervision, Funding acquisition. **Qinbai Yun:** Writing – review & editing, Supervision, Funding acquisition. **Wenbin Cao:** Supervision, Funding acquisition. **Qipeng Lu:** Writing – review & editing, Supervision, Funding acquisition, Conceptualization.

Declaration of competing interest

The authors declare that they have no known competing financial interests or personal relationships that could have appeared to influence the work reported in this paper.

Acknowledgments

This work was financially supported by the Beijing Natural Science Foundation (No. 2242008), the National Natural Science Foundation of China (Nos. 52471220, U2441264 and 51972026), the Fundamental Research Funds for the Central Universities (Nos. GJRC2023003 and 00007826), and the Guangdong Basic and Applied Basic Research Foundation (Nos. 2023A1515110010 and 2024A1515012653). This work was also supported by the National Key Research and Development Program of China (No. 2021YFF0704705), Major Research Plan of National Natural Science Foundation of China (No. 92263205), Scientific Equipment Development Project of Chinese Academy of Sciences, Youth Innovation Promotion Association Project of Chinese Academy of Sciences (No. 2020026), and Technical Support Talent Project of Chinese Academy of Sciences.

Supplementary materials

Supplementary material associated with this article can be found, in the online version, at doi:10.1016/j.cclet.2025.111974.

References

[1] J. Chow, R.J. Kopp, P.R. Portney, Science 302 (2003) 1528–1531.
[2] J. Chang, G. Wang, X. Chang, et al., Nat. Commun. 14 (2023) 1346.
[3] A. Kowal, M. Li, M. Shao, Nat. Mater. 8 (2009) 325–330.
[4] Q. Yun, Q. Lu, C. Li, et al., ACS Nano 13 (2019) 14329–14336.
[5] X. Zhou, Y. Ma, Y. Ge, et al., J. Am. Chem. Soc. 144 (2022) 547–555.
[6] G. Liu, W. Zhou, Y. Ji, et al., J. Am. Chem. Soc. 143 (2021) 11262–11270.
[7] Y. Chen, Z. Fan, Z. Luo, et al., Adv. Mater. 29 (2017) 1701331.
[8] P. Li, J. Bi, J. Liu, et al., J. Am. Chem. Soc. 145 (2023) 4675–4682.
[9] Y. Wang, M. Zheng, Y. Li, et al., Angew. Chem. Int. Ed. 61 (2022) e202115735.
[10] Y. Lv, P. Liu, R. Xue, et al., Adv. Sci. 11 (2024) 2309813.
[11] G. Qin, Y. Hao, H. Ma, et al., Adv. Funct. Mater. 34 (2024) 2312744.
[12] C. Ma, H. Zhang, J. Xia, et al., J. Am. Chem. Soc. 146 (2024) 20069–20079.
[13] L. Gao, X. Li, Z. Yao, et al., J. Am. Chem. Soc. 141 (2019) 18083–18090.
[14] G. Wu, W. Zhang, R. Yu, et al., Angew. Chem. Int. Ed. 63 (2024) e202410251.
[15] X. Cao, Y. Tian, J. Ma, et al., Adv. Mater. 36 (2024) 2309648.
[16] M. Armbrüster, K. Kovnir, M. Behrens, et al., J. Am. Chem. Soc. 132 (2010) 14745–14747.
[17] Y. Zhang, X. Liu, T. Liu, et al., Adv. Mater. 34 (2022) 2202333.
[18] M. Song, Q. Zhang, T. Shen, G. Luo, D. Wang, Chin. Chem. Lett. 35 (2024) 109083.
[19] B. Xu, T. Liu, X. Liang, et al., Adv. Mater. 34 (2022) 2206528.
[20] W. Tong, B. Huang, P. Wang, et al., Angew. Chem. Int. Ed. 59 (2020) 2649–2653.
[21] W. Xiao, M.A.L. Cordeiro, G. Gao, et al., Nano Energy 50 (2018) 70–78.
[22] B. Chen, P. Duan, S. Wang, et al., J. Mater. Chem. A 13 (2025) 17242–17260.
[23] J.A. Dean, Lange's Handbook of Chemistry, McGraw-Hill, Inc., New York, 1999.
[24] M. Zhou, J. Liu, C. Ling, et al., Adv. Mater. 34 (2022) 2106115.
[25] Y. Zhang, G. Li, Z. Zhao, et al., Adv. Mater. 33 (2021) 2105049.
[26] J.N. Hausmann, M. Ashton, S. Mebs, et al., Small 20 (2024) 2309749.
[27] C. Bianchini, P.K. Shen, Chem. Rev. 109 (2009) 4183–4206.
[28] Y. Xiong, J. Dong, Z.Q. Huang, et al., Nat. Nanotechnol. 15 (2020) 390–397.
[29] H. Lv, L. Sun, Y. Wang, S. Liu, B. Liu, Adv. Mater. 34 (2022) 2203612.
[30] Q.H. Wu, S.G. Sun, X.Y. Xiao, Y.Y. Yang, Z.Y. Zhou, Electrochim. Acta 45 (2000) 3683–3690.
[31] Z.X. Liang, T.S. Zhao, J.B. Xu, L.D. Zhu, Electrochim. Acta 54 (2009) 2203–2208.
[32] S. Han, H. Sun, C. Ma, et al., Adv. Funct. Mater. 34 (2024) 2403023.
[33] C. He, C. Ma, J. Xia, et al., Adv. Funct. Mater. 34 (2024) 2311683.
[34] B. Fei, Z. Chen, J. Liu, et al., Adv. Energy Mater. 10 (2020) 2001963.
[35] L. Ji, H. Che, N. Qian, et al., Appl. Catal. B: Environ. 328 (2023) 122521.